Intrinsic local symmetry breaking in nominally cubic paraelectric math xmlns="http://www.w3.org/1998/Math/MathML">mrow>mi >BaTi/mi>msub>mi mathvariant="normal">O/mi> mn>3/mn>/msub>/mrow>/math>

Xin-Gang Zhao, Oleksandr I. Malyi, Simon J. L. Billinge, and Alex Zunger

Phys. Rev. B **105**, 224108 — Published 10 June 2022

DOI: 10.1103/PhysRevB.105.224108

Intrinsic local symmetry-breaking in nominally cubic paraelectric $BaTiO_3$

Xin-Gang Zhao,[1] Oleksandr I. Malyi,[1] Simon J.L. Billinge,[2] and Alex Zunger[1,*]

1. Renewable and Sustainable Energy Institute, University of Colorado, Boulder, Colorado 80309
2. Department of Applied Physics and Applied Mathematics, Fu Foundation School of Engineering and Applied Sciences, Columbia University, New York, NY 10027
*Corresponding author email: Alex.Zunger@colorado.edu

Whereas at low-temperatures ferroelectrics have a well understood ordered spatial dipole arrangement, the fate of these dipole configurations in the higher temperature paraelectric (PE) phase remains poorly understood. Using density functional theory (DFT), we find that unlike the case in non-polar ABO_3, perovskites such as cubic $BaZrO_3$ that do not lower their energy by any form of positional symmetry breaking, the origin of distribution of the B-site off-centering in cubic PE such as $BaTiO_3$ is an intrinsic, energy lowering due to symmetry-breaking. Minimizing the internal energy E_0 of a constrained cubic phase represented by a large enough supercell to accommodate symmetry breaking already reveals the presence of a distribution of local displacements (i.e., a polymorphous network) in E_0 that (i) *locally* mimics the symmetries of the low temperature phases, while (ii) being the precursors of what finite-temperature DFT Molecular Dynamics (MD) finds as thermal motifs when equilibrating the free energy E_0 - *TS*. Analyzing the DFT-derived configurations of the PE cubic supercell by projecting its displacements onto irreducible representations reveals that it is best described as a temperature-dependent superposition of numerous modes, including ferroelectric (Γ_4^-) and antiferroelectric (M_2^- and X_5^+), rather than a single mode, (e.g., X_5^+) representing a well-defined long-range ordered configuration. This suggests that the electronic and dielectric properties of such PE phases are best calculated from a polymorphous distribution of inter-related local motifs in large supercells rather than from either purely disordered or long-range ordered models. In this respect, PE phases share a common feature with paramagnetic (PM) and paraelastic (PEL) perovskite phases whose central feature is a polymorphous distribution of local motifs —dipole moments in PE, magnetic moments in PM, and ordinary octahedral distortion modes in PEL—all computable by DFT supercells and useable in calculating electronic and magnetic properties of para phases.

Oxide perovskites ABO_3, typified by $BaTiO_3$ (BTO), have local dipoles $\{\mu^{(i)}_{local}\}$, formed by polar atomic displacements off high symmetry positions *i*. At low temperatures, these can organize into ferroelectric (FE) long-range-ordered (LRO) structures. Above the Curie temperature T_C ~401 K, BTO transforms into a cubic PE phase, [1] whose microscopic configuration is poorly understood. Crystallographically, this high-temperature PE structure, as well as that of the experimentally reported ~90 other perovskite oxide [2,3] and scores of halide perovskites, [4,5] are classified as Pm-3m space group symmetry with a single formula unit per cell. A central question in this field [6–16] regards the nature of the spatial configurations of the local $\{\mu^{(i)}_{local}\}$ dipoles in such PE phases. Suppose the Pm-3m paraelectric phase, consisting of a single, undeformed octahedral motif as its repeat unit (the monomorphous configuration), is taken literally rather than as a 'virtual crystal' average over configurations. In this case, the PE phase will not only have vanishing global dipole moment μ_{global}~0, but also vanishing local dipoles on each site, $\{\mu^{(i)}_{local}=0\}$ (a 'non-electric' configuration; Fig. 1a insert). Experimentally, in contrast, the pioneering 1968 diffuse scattering XRD measurements of Comes et al. [9] on the PE phase were interpreted as being due to the presence of nonzero local dipoles $\{\mu^{(i)}_{local}\}$ that persist locally in the high-temperature cubic phase of BTO. Other measurements also seem to indicate the off-centering of the Ti ions not only in the low-temperature FE phases but also in the PE phase. This includes Nuclear Magnetic Resonance (NMR), [10] atomic pair distribution function (PDF) analysis of neutron powder diffraction data, [11–13] X-ray absorption fine structure (EXAFS), [14] as well as the observation of birefringence, [17] second harmonic generation (SHG), [18] and piezoelectricity in cubic oxide paraelectrics. [19,20] The SHG and piezoelectricity effects, however, are forbidden in the centrosymmetric nominal cubic phase, suggesting that locally the symmetry in PE BTO is non-centrosymmetric. Although some sightings of such 'forbidden symmetries' appear to involve *extrinsic* factors (such as defects [21] or growth-induced non-ideal microstructures [22]), there are cases, most prominently BTO, [23] where *intrinsic symmetry-breaking* appear to be at play. Other experiments, the most notably inelastic neutron scattering, [24,25] suggest that the local dipoles appear only on cooling through the FE phase transition. The resulting controversy has held the perovskite community in fascination for over 50 years. This dilemma can be posed in the following way: Is the PE condition of μ_{global}~0 realized by having (a) $\{\mu^{(i)}_{local}=0\}$ (symmetry unbroken, absence of local dipoles, as illustrated in Fig. 1a insert) or (b) via distribution of mutually compensating nonzero local dipoles $\{\mu^{(i)}_{local}\neq 0\}$ (Fig. 1d insert). What makes the resolution of this conundrum important is that the choice between (a) vs. (b) strongly affects the nature of predictions of calculations of spectroscopic and transport properties. For example, the use of the monomorphous view (a) ubiquitous in standard databases [26–29] as input to calculations often leads to a significant underestimation of band gaps. [30–33] Analogous dilemma exists in interpreting the nature of the distribution of local moments in paramagnetic (PM) phases of magnetic oxide perovskites, where assumes the view of a minimal Pm-3m unit cell with a single formula unit, common in electronic structure calculations of PM, leads to well-known contradictions with data.

On the other hand, possibility (b) has been generally interpreted by attributing local dipoles in the PE phase to *thermal fluctuations*, where atoms are oscillating thermally around their Wyckoff positions and time averaging to a zero polarization. However, such thermal effects do not account for the intrinsic nature of the polarization implied by the macroscopic experiments. [34] Indeed, there is also a possible contribution from modes driven by intrinsic effects (such as the nature of the chemical bonding in such phases) even before thermal motion sets in. Such intrinsic, a-thermal symmetry breaking are known in inorganic compounds, such as degeneracy removal exemplified by the Jahn-Teller distortions of *d* orbital impurities in insulators, [35] or by the lone-pair *s* orbitals of Sn, Pb, or Bi centers in inorganic compounds, [36] or via sterically-induced octahedral rotations and tilting in perovskites, [37] all understood as a-thermal energy lowering symmetry-breaking that can exist prior to thermal agitation.

The present work offers a different view on the *origin and properties* of the microscopic structure of PE phases, using as an example the classic cubic PE $BaTiO_3$. We start with first-principles energy minimization of the *internal energy* E_0 followed by a finite-temperature MD simulation of its free *energy* $F = E_0 - TS$. The computational details used for internal energy minimization, as well as the description of the different exchange-correlation (XC) functionals and the finite-temperature MD simulation, are explained in Appendix A and B.

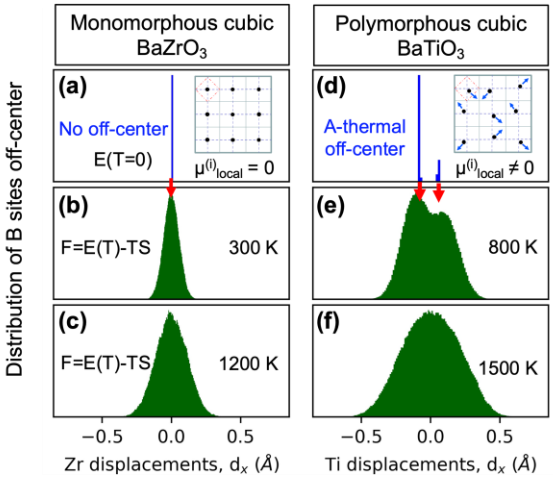

Figure 1. (XC=PBE) Distribution of projected B site displacements d_x in ABO_3 with respect to the center of mass of an octahedron is shown for the cubic $BaZrO_3$ in (a-c), and the intrinsically symmetry-breaking cubic $BaTiO_3$ (in d-e). Inserts in (a, d) are the schematic illustrations of the B atomic displacements in models of cubic monomorphous and polymorphous structures. The displacements were taken from ~20,000 snapshots on equilibrated MD trajectories with *NPT* ensemble (N=64 fu/cell; P=1 atm; Δ t=1 fs). The a-symmetry in (e) with respect to Ti displacements changed by less than 10% by increasing the simulation times of 20, 40, and 60 ps (see detailed discussion in Appendix C).

We find that the displacement pattern in the finite temperature cubic PE phase evident in MD simulations follows a blueprint encoded already by the a-thermal symmetry-breaking that emerges from a constrained minimization of the internal energy E_0 for a cubic phase. As a reference point, we recall that conventional 'monomorphous' compounds such as Si, GaAs, or $BaZrO_3$ (the latter shown in Fig 1(a-c)) are not stabilized by intrinsic symmetry-breaking and thus give the same calculated result per atom if a small unit cell of a given symmetry is used, or a larger supercell replica. However, in the PE cubic phase of $BaTiO_3$, the resulting 'polymorphous network' exhibits a pattern of intrinsic, a-thermal off-center displacements (shown by the blue lines in Fig. 1(d) and the leading red arrows. As temperature rises (Fig. 1(e)), the underlying polymorphous pattern in BTO is initially retained at intermediate temperatures before it is overwhelmed by strong thermal motions at much higher temperatures (Fig. 1(f)). The latter displacement pattern is now centered symmetrically at the zero-displaced position, akin to a behavior characteristic of conventional monomorphous compounds (Fig. 1(a-c)) at *all temperatures.*

Compared with using 'monomorphous' Pm-3m configuration, the displacement patterns show better agreement with the measured PDF. [11–13] The distributed intrinsic symmetry-breaking is enabled only if one allows a larger than minimal high symmetry unit cell which has the geometric flexibility to break symmetry—should the internal energy E_0 be lowered.

The emergence of such a polymorphous network consisting of an energy lowering distribution of local environments is a fundamentally important result with broad implications. It is an example where allowing the structure to have symmetry lowering distortions, even whilst respecting the global, 'average' cubic symmetry, that DFT can find *intrinsic symmetry broken structures that lower the energy of the system*. They are intrinsic in the sense that the distortions are not a result of extrinsic imperfections such as defects or doping. We believe that not all structures, but many structures will do this, especially ones with high susceptibilities to various applied forces such as the ferroelectrics discussed here. It not only explains poorly understood experimental observations in BTO but more broadly gives us a recipe for finding new functional materials by using DFT to search for previously unknown polymorphous network materials. In this respect, PE phases share a common feature with paramagnetic (PM) and paraelastic (PEL) perovskite phases whose central feature is a polymorphous distribution of local motifs—dipole moments in PE, magnetic moments in PM, and ordinary octahedral distortion modes in PEL—all computable by DFT supercells and useable in calculating electronic and magnetic properties of para phases.

The present approach to the microscopic understanding of para-phases allows us to learn a great deal about symmetry-breaking. For example, upon projecting the displacement field on the irreducible representation, we find the *hidden polar FE-like mode* Γ_4^- with given 4×4×4 supercell, forbidden in the nominal cubic structure but consistent with the experimentally observed SHG [18] and piezoelectricity [19,20] that are disallowed in centrosymmetric (e.g., Pm-3m) phases. It is significant that the MD study using the classic force field (lacking explicit electronic degrees of freedom) demonstrates [16] at temperature above T_c a symmetric displacement field, producing zero net polarization. Furthermore, in contrast to

commonly used approximations [38] that describe PE phases as an *averaged* high-symmetry cubic structures that are *non*-electric (vanishing global polarization because all local dipoles are also zero), we deduce that neither averaged monomorphous cubic Pm-3m (used in 1000s of previous studies), nor as a long-range ordered cubic anti-ferroelectric (AFE) phase with single type AFE mode [39,40] commonly invoked is the universally physical model to describe the structural properties and electronic structure of PE phases.

Theoretical approach: To understand the possible significance of symmetry-breaking within the PE phase and whether it emerges from intrinsic or thermal effects, we use a polymorphous DFT (polyDFT) approach. [41,42] In brief, it (i) does not restrict the *local* symmetry of the PE phase to that of a monomorphous Pm-3m structure having a single local motif, (ii) does not use a long-range-ordered dipole model for the PE phase that has fixed Wykoff positions in given cubic space group, [39,40] and (iii) explores both intrinsic (via minimization of the internal energy E_0) and dynamic (via thermal evolution of the free energy $F=E_0 - TS$ in first-principles molecular dynamics). To allow unimpeded local symmetry-breaking whilst respecting the *global* cubic symmetry, we constrain the lattice vectors to the macroscopically observed cubic shape a=b=c but allow internal symmetry breaking if it lowers the energy (another choice, not used here, is to constrain both the cubic cell shape and the internal atomic positions to cubic symmetry [39,40]). We use enlarged unit cells (here, 64 formula units (fu), i.e., 320 atoms; the results are rather stable against further cell enlargement). Table I (Appendix B) demonstrates the rather weak dependence of the result on the initial configuration and on the random atomic nudges used to initialize the minimization.

The results are analyzed to study the correlation between different displacements by projecting the displacement field on irreducible representations as did in Duyker et al. [43] We do so via DFT that retains explicit electronic and lattice degrees of freedom. Whereas using a first-principles description limits supercell size and simulation time, the appearance of an active irreducible representation mode Γ_4^- shown in Fig. 3 at all temperatures clearly predicts correlated displacements, which is consistent with net polarization ~0.02 Å at 800 K and ~0.01 Å at 1200 K. However, it does not capture the few nm-scale correlated displacements that have been reported experimentally near T_c. [9]

The distribution of Ti-O atomic pairs in paraelectric phase (Fig. 2): We consider the partial radial distribution function (PRDF), $g(r)_{ab}$, between species *a* and species *b*, defined as

$$g(r)_{ab} = \frac{1}{N_a}\sum_{i=1}^{N_a} \frac{\sum_{j=1}^{N_b}\langle\delta(|r_{ij}-r|)\rangle}{4\pi r^2 dr} \qquad (1)$$

where N_a and N_b refer to the total number of atoms for each species and r_{ij} is the length of the vector from atom *i* to atom *j*. The PRDF of Ti-O pairs in the ground FE rhombohedral structure is shown in Fig. 2(a) and compared with the results of the polymorphous PE cubic network with intrinsic distortion (blue lines Fig. 2(b)) and with snapshots at 800 and 1200 K of the MD profile (Fig. 2(c, d)). Significantly, we find, in the polymorphous cubic PE phase, a splitting of the nearest-neighbor Ti-O peak (Fig. 2(b)). This splitting is due to the emergence of the set of local Ti off-center displacements (Fig. 2(b)). No constraint is placed on the directions of symmetry lowering displacements in the DFT calculations, which are guided simply by lowering the internal energy. However, we note that the displacements occur predominantly along {111} directions, which is consistent with the ground-state rhombohedral structure and the experimental observations of local structural probes, [9,11,14] resulting in the formation of three short (1.88 Å) and three long (2.13 Å) Ti-O bonds. A remnant of the nearest-neighbor Ti-O bond splitting is also observed in PRDFs obtained from our finite temperature MD calculations at temperatures of 800 and 1200 K (green lines shown in Fig. 2(c, d)), presenting a large a-symmetry peak. Interestingly, the polymorphous cubic PE phase also has local structural motifs that are not present in either the nominal cubic monomorphous approximant (Fig. 2(e)) or the low-temperature FE phase (Fig. 2(a)). However, the PRDF of other pairs in the polymorphous network (Appendix D) shows relatively small broadening in the range of 1-8 Å but no apparent asymmetry of the first-nearest peaks. This might be because of the Goldschmidt tolerance factor[43] $t_{eff} = \frac{R_A+R_O}{\sqrt{2}(R_B+R_O)}$ of cubic BTO (1.06) is slightly larger than one, so octahedral tilting/rotation or A site displacements are small.

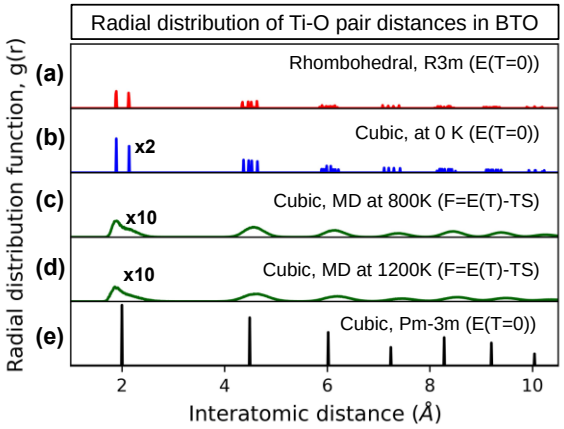

Figure 2. (a-e) Ti-O RPDF before and after temperature set in (XC=PBE). Here, (a) is the RPDF for the intrinsic rhombohedral phase (1fu/cell), (b) is for the intrinsic polymorphous network, and (c) and (d) are from 100 snapshots equilibrium trajectories of MD simulation in the NPT ensemble at 1 atm, 800 and 1200 K with interval 0.1 ps. Finally, (e) shows RPDF in nominal cubic phase (1 fu/cell).

Local symmetry-breaking driven by the internal energy: The characteristic of a polymorphous [41,42,45] structure of a material is that the total energy per atom in a supercell constrained to have the same shape as the macroscopically observed "average structure" is seen to initially decrease as the supercell size increases before saturating at a certain supercell size. We find that ***cubic*** BTO is polymorphous (average energy reduction -24±2 meV/fu (PBE) relative to the monomorphous approximation), with predominantly Ti off-center displacements (Fig. 2 (b)). Not all materials are polymorphous, as shown in Fig. 1(a): the non-paraelectric $BaZrO_3$ has only thermal motion. Indeed, we find that this is the case for BTO in its ground-state rhombohedral structure (R3m, SG:160), where there is no symmetry-breaking

induced intrinsic energy reduction on increasing the cell size.

The decomposition of intrinsic and dynamic distortion fields in terms of irreducible representations of the cubic Pm-3m symmetry (Fig. 3): The polyDFT calculations show a local symmetry-breaking in cubic BTO, although this calculation step excludes any effects due to the finite temperature. This points to an intrinsic energetic driving force for forming local distortions under the set of constraints given. It is interesting to inquire what is the *origin* of the intrinsic symmetry-breaking mode symmetries in the PE phase. We find that these symmetries are inherited from the low-temperature long-range ordered FE phase as well as theoretically predicted long-range ordered cubic AFE phase with zero net total dipole, [39,40] albeit without the long-range dipolar order, as indicated by their irreducible representation modes in Fig. 3(a) and 3(b) (computational details are provided in Appendix A). Specifically, the low-temperature FE rhombohedral phase is a condensation of just one of these modes—the one associated with the Γ_4^- irrep (Fig. 3(a)), —whereas the predicted AFE phase is associated with M_2^- irrep. The intrinsic polymorphous model of the PE phase shows that the projected Γ_4^- irrep mode is still one of the most prominent modes (Fig. 3(c)) at T=0, resulting in a Ti off-centering that is almost as large (0.09 Å) as in the rhombohedral phase (0.20 Å). However, the Γ_4^- is not the only significant mode that is populated in the polymorphous network. Five additional modes—X_5^+, Σ_3, M_2^-, Z_2, and Δ_5—all with AFE patterns have significant amplitudes. These modes originate from relative Ti displacements along opposite {100} directions in different TiO_2 layers. For example, for X_5^+, the AFE-like Ti displacements occur in adjacent TiO_2 layers, whereas for Δ_5, the AFE-like Ti displacements occur in three TiO_2 layers, in which the Ti displacements in the middle TiO_2 layer are not displaced. These additional X_5^+, Σ_3, M_2^-, Z_2, and Δ_5 modes have distortion magnitudes in the range of 0.04-0.10 Å. Importantly, they robustly appear in all independently restarted polymorphous calculations (Table I in Appendix B), suggesting they are a robust part of the polymorphous state and not due to incomplete sampling. Since Δ_5, Σ_3, M_2^-, Z_2, and X_5^+ are absent in the globally rhombohedral phase, presumably, they play a role in relaxing the local distortion.

Thermal effects on paraelectric modes and Ti distributions: To capture thermal effects, we use MD simulations starting from the intrinsic polymorphous results. The MD runs result in atomic configurations that can also be decomposed onto the basis of the distortional modes of irreps as was done for the polyDFT relaxed structures in Fig. 3(c). As expected, as the temperature is raised, many additional modes become significantly populated. For example, the mode population averaged over 100 snapshots (within 10 ps timescale) in MD simulation at 800 and 1200 K are shown in Fig. 3(d, e), indicating that the Γ_4^-, M_2^-, and X_5^+ symmetry modes remain active even at 1200 K, i.e., well into the PE phase, despite the fact that new modes join in the symmetry-breaking and the relative magnitude of each mode is temperature dependent. Further, the projected Ti displacements at 800 and 1200 K (see Supplementary B) also indicate that the off-center distortion, though prominently off-center contribution at 800 K seems to be gradually overcome as temperature increases to 1200 K, being close center-flat-like distribution. The center-flat-like distribution has been observed based on the MD simulation with a force field and interpreted as mixed character of "order-disorder" and "displacive" [15,16] near T_c. Indeed, Pasiak et al. [16] found that the on-center population of Ti atoms is shallow at T_c + 100 K. Therefore, the vector of off-center might be changed due to thermal effect, but never be dominated population at zero as in cubic polymorphous network at T=0 K.

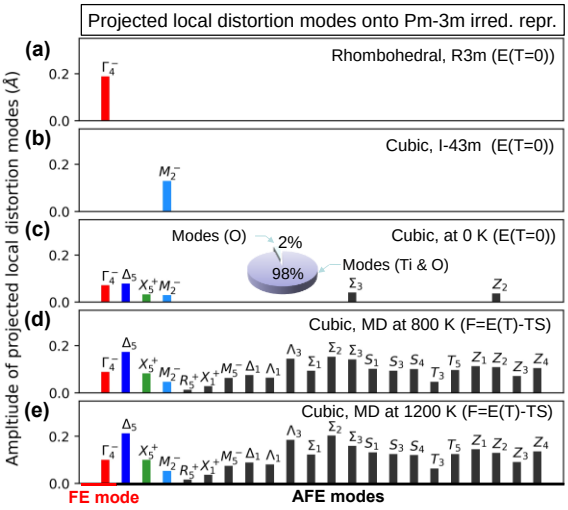

Figure 3. (XC=PBE) Projected distortion modes related to Ti and oxygen intrinsic- & thermal- displacements onto parent undistorted cubic (Pm-3m) irreducible representations of (a) ground state rhombohedral structure, (b) *ordered* AFE cubic phase (I-43m), (c) supercell structure with the distributed intrinsic distortions, and (d, e) snapshots on equilibrated MD trajectory. Insert to (c) shows the indicated modes projected onto atomic displacements. The heights of bars in (c, d, and e) refer to the averaged amplitude for each of the 10, 100, and 100 configurations, respectively. The 10 configurations in (c) are obtained from 10 independent runs starting from the re-nudged supercell structures (see Table I). Each of 100 configurations in (d, e) are extracted with interval 0.1 ps from the equilibrated MD trajectory with NPT ensemble at 800 and 1200 K, pressure 1 atm, and timestep 1 fs. Γ_4^- is a FE-like Ti displacements, whereas the rest of the mode are AFE-like relative Ti displacements.

The net polarity in the paraelectric phase and its dependence on temperature (Fig. 3): The projections described above give important insights into the nature of the collective distortion modes of the system, but it gives incomplete information about the polarizability of the material. To quantify this, we need to consider the size of the local electric dipoles $\{\mu^{(i)}_{local}\}$, which are proportional to the displacements of Ti atoms away from the center of their local O_6 octahedral hosts. These Ti displacements can be represented with respect to the mass center of the octahedron in polymorphous structures and MD snapshots. The projections of Ti displacements along <100> direction is shown in Fig. 1(e, f) for 64 fu supercell for different temperatures, showing the presence of Ti-off-centering. This effect has been ascribed previously to the thermal effect, [16] but it emerges here from the static calculation, suggesting the origin is electronic symmetry-breaking associated with this energy lowering. The ensuing intrinsic net polarization is ~0.15±0.01 Å (XC=PBE) oriented close to <111>

direction before temperature set in. Further, by averaging all dipoles $\left|\sum_1^N \vec{d}\right|$ over a ~40 ps period on the equilibrium MD trajectories, we find that the global dipole is diminished with temperature: μ_{global}=0.02 and 0.01 Å at 800 and 1200 K, respectively. This nonzero global polarization is due to the Γ_4^- mode (Fig. 3) with a local FE-like pattern in a 4×4×4 supercell, which is different from predicted long-range ordered cubic $BaTiO_3$ with zero net dipole. [39,40] In our calculation, the net global polarization around T_c is not zero, in agreement with the measured polarization of single crystal BTO above T_c. [46,47] This nonzero polarization might contribute to anomalous observations, such as Raman splitting, [48] SHG, [18] piezoelectricity [19,20] and seen in PE cubic BTO. As shown in Fig. 1(e, f), Ti displacements change off-center to on-center vibration as temperature increases from 800 to 1200 K (also see Appendix C). The off-center Ti displacements are observed at 1200 K. We note that the temperature at which such displacements can be observed might be overestimated because of the overestimated lattice expansion by PBE functional. This finding is different from the general understanding (i.e., above T_c, the PE phase is described by the displacive model [47] as a single parabolic well, lacking static displacements) of the PE phase at finite temperatures.

We conclude that in addition to the usual thermally-driven disorder in conventional compounds such as $BaZrO_3$, other compounds such as PE $BaTiO_3$ manifest an *intrinsic* a-thermal precursor to symmetry-breaking in the form of a ('polymorphous') distribution of energy-lowering local motifs. These can survive at finite temperatures in the PE phase, providing a physical understanding of the microscopic structures and their anomalous phenomenon in these kinds of PE materials.

Acknowledgements:
We thank fruitful discussions with Ekhard K. H. Salje and Annette Bussmann-Holder on paraelectrics, Zhi Wang on the long-range-order model of AFE, and Lin Ding Yuan for assistance in calculating polymorphous structures with different initial nudges shown in Table I (Appendix B). The work in the Zunger's group and Billinge's group was supported by the US National Science Foundation through grant DMREF-1921949. The calculations were done using the Extreme Science and Engineering Discovery Environment (XSEDE), which is supported by the National Science Foundation grant number ACI-1548562.

Appendix A. Computational details

All the structural optimizations were carried out using the Density Functional Theory (DFT) within ionic pseudopotential and plane-wave basis set with the Perdew-Burke-Ernzerhof. (PBE) [49] exchange-correlation (XC) functional, as implemented in the VASP code. [50,51] The valence electron configurations for creation of the ionic pseudopotentials were Ba($5s^25p^66s^2$), Ti($3d^34s^1$), O($2s^22p^4$), and Zr($4s^24p^64d^35s^1$), respectively. The energy threshold was set to $1x10^{-6}$ eV/cell, the force on each atom was converged to < 0.01 eV/Å. All the *ab initio* calculations managements and data post-processing were done using an open resource named JAMIP program. [52]

Internal energy minimization: A 12×12×12 k-mesh was used to get 1 fu/cell structure lattice constants by keeping global Pm-3m symmetry. The 4×4×4 supercells with initial nudges (0.01 Å with random direction) were roughly optimized using Gamma-only k- point grid within frozen out-shape and lattice constants of the supercell, then the force on each atom was carefully relaxed with 3×3×3 k-point grid. To get the accurate differences of total internal energy between undistorted structure (called nominal cubic) and optimized supercell (called polymorphous), we calculated the internal energies of all the structures with the same cell size (4×4×4 supercells) and K-grid (3×3×3 k-mesh) using PBE [49] (For comparison, XC=SCAN [53] that gives more accurate of total energy is also considered) functional as shown in Table I Appendix B.

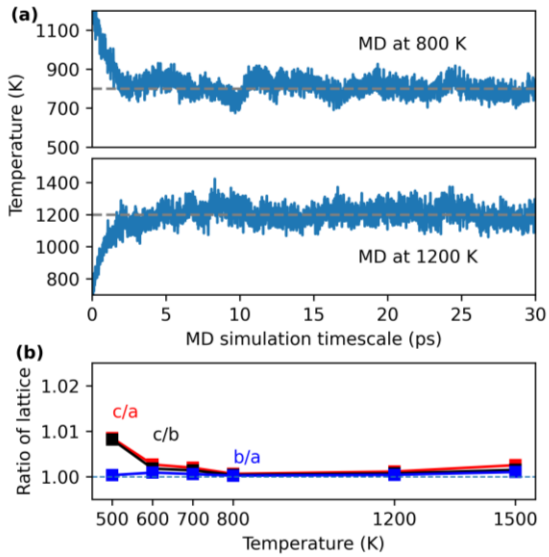

Figure 4. (a) Temperature fluctuation as a function of MD simulation time for 800 and 1200 K. (b) The ratio of lattice constants of BTO as temperature increases. The lattice constants a, b, and c at each temperature are the averaged values of lattice constants for all the snapshots within 10 ps MD simulations trajectory when temperatures reach the initially set constant value.

Ab initio Molecular Dynamic simulations (AIMD) and prediction of Curie temperature: To study the local symmetry-breaking at finite temperatures, we carried the AIMD using 4×4×4 supercell (64fu/cell) with polymorphous nature, PBE functional, Gamma-only K-grid, and NPT ensemble (Langevin thermostat [54]) at 500, 600, 700, 800, 1200, and 1500 K, respectively (the measured Curie temperature and melting point for cubic $BaTiO_3$ is T_c = 401 K [11] and 1893 K, [55] respectively). The friction coefficients using a Langevin thermostat are set to 1 ps^{-1} for Ba, Ti, Zr, and O atomic degrees-of-freedom and 100 ps^{-1} for lattice degree-of-freedom. The time step is set to 1 fs.

The ideal Pm-3m $BaTiO_3$ has lattice constant c/a==1. The experimentally measured c/a value of the tetragonal phase lattice constant is ~1.010, [56] and values extracted from the MD simulation, and DFT calculation is ~1.026. [15] Here, the Curie temperature from tetragonal to cubic phase is

estimated by checking the ratio of lattice constant c/a at different temperatures without considering the atomic positions.

As shown in Fig. 4(a), the temperature reaches the constant value after ~10 ps at 800 and 1200 K starting from the DFT polymorphous kernel configurations (4×4×4 supercell). Therefore, the statistical analysis (e.g., Ti displacements, lattice constants) of AIMD simulations at finite temperatures shown in all figures is based on the snapshots on the equilibrated trajectories after 10 ps. As shown in Fig. 4(b), the AIMD simulation reveals that there is a relatively sharp change of the c/a value from 1.004 at 600 K to 1.020 at 500 K. Therefore, we propose that the Curie temperature from tetragonal to cubic phase for $BaTiO_3$ is roughly between ~500 and ~600 K based on our input parameters with NPT ensemble at 1 atm in a 4×4×4 supercell.

Projected Ti displacements: In $BaTiO_3$, we define the off-center displacement for each Ti atom as a vector from the coordinates of the virtual mass center C_i^0 of the host octahedron O_6 to the coordinates of the actual Ti position C_i in the Cartesian coordinate, expressed $\vec{d} = C_i - C_i^0$, where the i=1-64 is the index of Ti in the 64 fu/cell. The vector is projected to the <100>, <010>, and <001> directions, which is defined as d_x, d_y, and d_z, respectively. The detailed discussion on projected Ti displacements is addressed in Appendix C.

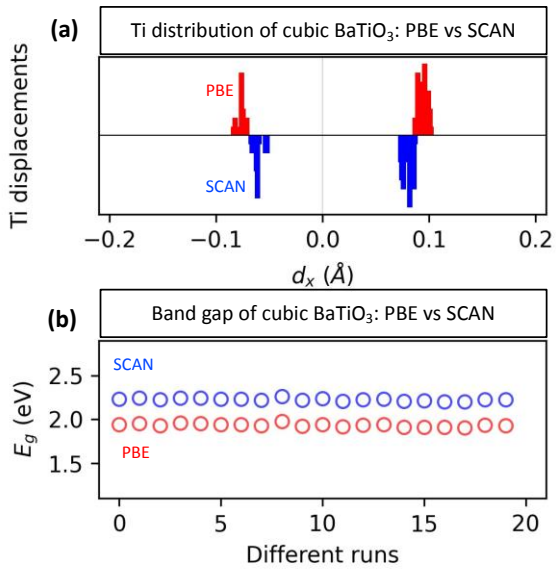

Figure 5. Comparison of Ti displacements in polymorphous structure ID#20 and band gaps of 20 cubic polymorphous structures using PBE and SCAN functionals.

Projected irreducible representation modes on Pm-3m symmetry: This analysis involves describing a low symmetry structure as arising from the parent high symmetrized structure with one or more static structural distortions. [57] The undistorted parent structure has zero amplitudes for all the potential structural distortion modes described by the irreducible representation of the high-symmetry structure. In low symmetry structures, structural distortion modes with nonzero amplitudes are called active modes. This analysis can isolate the distortions in a low symmetry structure with complex local distortions and provide the contribution of active modes by comparing their amplitudes. The projected distortions to the adapted symmetry mode in the nominal cubic structure were obtained using ISOTROPY software. [58] The distortion modes with amplitude > 0.01 Å are ordered from mode with the largest amplitude to the smallest amplitude in Table I (Appendix B).

Appendix B. Comparison of energy minimization and by using different correlation functional

As shown in Fig. 5 and Table I, we find that the intrinsic symmetry-breaking occurs in all runs, resulting in total energy lowering with respect to undistorted cubic Pm-3m structure is -21 to -26 meV/fu (PBE) and -12 to -16 meV/fu (SCAN). Using different XC functionals does not qualitatively change the physical observation, i.e., symmetry breaking resulting in internal energy lowering and non-zero net Ti off-center displacements. Quantitively, the values of net off-center displacements, total energy lowering as well as band gap, and distribution of Ti atoms are shifted along the same direction when using different XC.

Table I. Properties of cubic $BaTiO_3$ with polymorphous nature from 20 runs. The net dipole is defined as the absolute value of the sum of displaced Ti vectors with respect to the mass center of the octahedron. Internal energy lowering of cubic $BaTiO_3$ is the enthalpy difference between the polymorphous configuration and the undistorted Pm-3m configuration. Configurations ID#01-10 are obtained starting from Pm-3m configuration with an initial random nudge (0.01 Å) on each atom. Configurations ID#11-20 structures are obtained starting from #04 by re-adding random nudge (0.01 Å) on each atom. All the configurations are obtained within the fixed lattice constants equal to optimized Pm-3m $BaTiO_3$. The irreducible representation modes with amplitude > 0.01 Å for each configuration and two long-range ordered cubic $BaTiO_3$ are also listed.

ID	Net dipole (Å)		Energy lowering (meV/fu)		Irrep. Modes (> 0.01 Å)
	PBE	SCAN	PBE	SCAN	
01	0.15	0.08	-24	-14	Γ_4^- Δ_5 X_5^+ M_2^- Σ_3 Z_2
02	0.15	0.05	-21	-12	
03	0.15	0.06	-23	-13	
04	0.16	0.06	-26	-15	
05	0.15	0.01	-22	-12	
06	0.15	0.03	-23	-13	
07	0.15	0.02	-23	-13	
08	0.15	0.04	-22	-12	
09	0.15	0.07	-23	-13	
10	0.15	0.03	-24	-14	
11	0.15	0.06	-24	-15	
12	0.16	0.08	-26	-16	
13	0.15	0.06	-24	-14	
14	0.15	0.08	-25	-15	
15	0.15	0.08	-26	-16	
16	0.15	0.06	-24	-14	
17	0.15	0.07	-25	-15	
18	0.15	0.07	-24	-14	
19	0.16	0.07	-26	-16	
20	0.15	0.05	-23	-14	
21	0.00	0.00	I-43m, Ref [39,40]		M_2^-
22	0.00	0.00	P-a3, Ref [40]		X_5^+

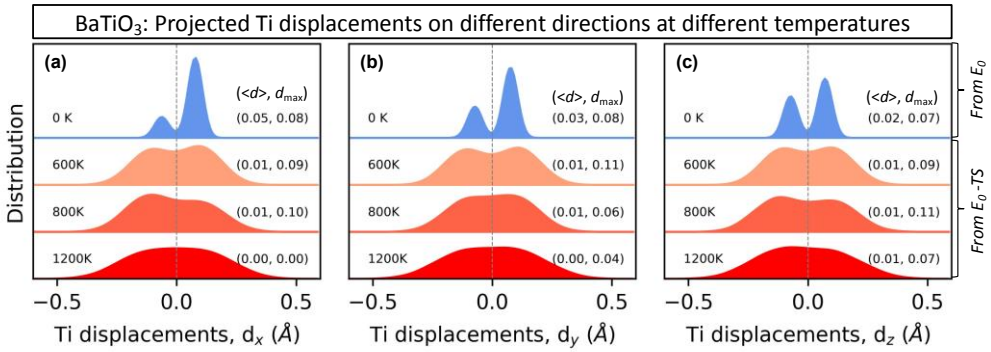

Fig. 6. (a-c) Distribution of the projected Ti displacements d_x, d_y, and d_z of configurations at different temperatures. The first row (in blue) is obtained by constrained minimization of the internal energy E_0 of a supercell with cubic lattice vectors but relaxed cell-internal atomic sites. Finite temperature resulted (in red) are from Molecular dynamics. All show symmetry breaking for T< 800 K, which is reduced at higher temperature to a flat featureless distribution, N = ~20,000 snapshots are used for obtaining the Ti displacements at 600, 800, and 1200 K as well as 10 configurations (i.e., ID#01-10, see Table I in Appendix B) with polymorphous nature before temperature set in (T=0). The values in the parathesis refer to amplitude of (*asymmetry*, *off-center*).

Appendix C. Projected Ti displacements in cubic $BaTiO_3$ before and after temperature sets in

Figure 6 shows the distribution of the projected Ti displacements along with d_x, d_y, and d_z in 10 (ID#01-10 in Table I Appendix B) structures obtained by minimizing internal energy E_0 and ~20,000 snapshots at different finite temperatures (XC=PBE).

Here, we use two quantities—amplitude of *off-center*, defined as $d_{max} \leftarrow \max(\sum_i^N \sum_j^{64} \delta(|d_{ij} - d_{max}|))$ and amplitude of *asymmetry* defined as $\langle d \rangle = \frac{\sum_i^N \sum_j^{64} d_{ij}}{64N}$, to quantitively evaluate the local Ti displacements.

We focus on two aspects here: (i) Symmetry breaking manifested by the off-center displacements in the PE phase being the central result, and (ii) the fact that the symmetry breaking is slightly asymmetric—a fact contributed in part most likely by numerical aspect.

(i) As shown in Fig. 6, the *off-center* d_{max} along d_x, d_y, and d_z in cubic $BaTiO_3$ is ~0.08 Å using the internal energy alone before temperature sets in, presenting two off-center peaks. The distribution of Ti displacements at 800 K mimics the polymorphous distribution seen in the supercell before temperature sets in, having d_{max} = ~0.10 Å. The two-peaks distribution gradually transforms to a flat and structureless distribution as temperatures increase above predicted Curie temperature, with a decrease of d_{max} from ~0.10 at 800 K to ~0.04 at 1200 K in the same time window (20 ps) and cell size (64fu/cell). The decrease of d_{max} at finite temperatures indicates that the thermal effects can suppress the off-center characteristic.

(ii)The *asymmetry of the two peak symmetry breaking plot in* the distribution of projected Ti displacements in Fig. 6 is ~0.03 when the internal energy alone is used, whereas the asymmetry at 800 K is smaller (~0.01) and is close to zero at 1200 K within 20 ps time window and 64 fu cell size. The amplitude of the *asymmetry* at 800 K is reduced (by <10%) but is not zero when considering the from 20 to 60 ps, pointing out that the simulation time (or the cell size) might be contributing factors to this asymmetry.

Appendix D. Partial radial distribution function (PRDF) in cubic $BaTiO_3$

Figure 7 shows PRDFs of the Ba-Ba, Ba-Ti, Ti-Ti, Ba-O, and O-O pairs in the nominal cubic, and in polymorphous cubic $BaTiO_3$ before and after temperature set in. The position of peaks along the nominal cubic, polymorphous structures are identical. However, the relative intensity of peaks in polymorphous structures at ~ 10 Å for Ba-Ba pairs, ~6.5 Å, and ~ 10 Å for Ti-Ti pairs, > ~ 5 Å for Ba-O pair and > ~2.5 Å for O-O pairs are not well agreement with the nominal cubic structure. Note that none of the pairs except Ti-O show significant asymmetry of the first peaks, indicating the existence of the locally off-center Ti.

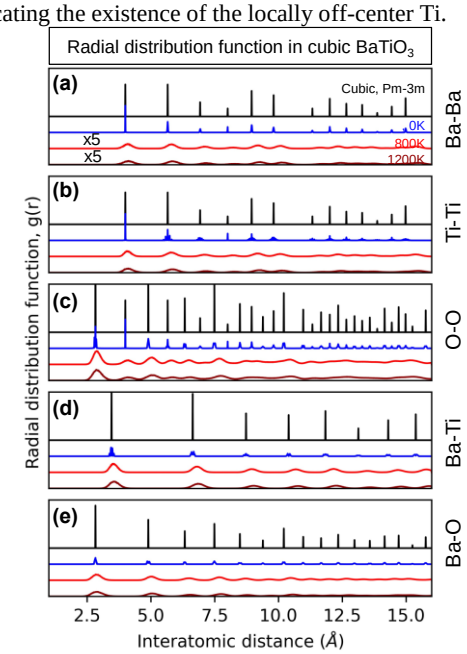

Figure 7. (a-e) Comparison of pair distributions (Ba-Ba, Ti-Ti, O-O, Ba-Ti, and Ba-O) among nominal cubic (SG: 221, black line), cubic $BaTiO_3$ with polymorphous nature (blue

curve) and MD snapshots at 800 K (red curve) and 1200 K (dark red curve).

References

[1] M. B. Smith, K. Page, T. Siegrist, P. L. Redmond, E. C. Walter, R. Seshadri, L. E. Brus, and M. L. Steigerwald, *Crystal Structure and the Paraelectric-to-Ferroelectric Phase Transition of Nanoscale $BaTiO_3$*, J. Am. Chem. Soc. **130**, 6955 (2008).

[2] C. J. Bartel, C. Sutton, B. R. Goldsmith, R. Ouyang, C. B. Musgrave, L. M. Ghiringhelli, and M. Scheffler, *New Tolerance Factor to Predict the Stability of Perovskite Oxides and Halides*, Science Advances **5**, eaav0693 (2021).

[3] P. V. Balachandran, A. A. Emery, J. E. Gubernatis, T. Lookman, C. Wolverton, and A. Zunger, *Predictions of New ABO_3 Perovskite Compounds by Combining Machine Learning and Density Functional Theory*, Phys. Rev. Materials **2**, 043802 (2018).

[4] J. Wiktor, U. Rothlisberger, and A. Pasquarello, *Predictive Determination of Band Gaps of Inorganic Halide Perovskites*, J. Phys. Chem. Lett. **8**, 5507 (2017).

[5] Q. Sun and W.-J. Yin, *Thermodynamic Stability Trend of Cubic Perovskites*, J. Am. Chem. Soc. (2017).

[6] K. A. Müller and W. Berlinger, *Microscopic Probing of Order-Disorder versus Displacive Behavior in $BaTiO_3$ by ${\mathrm{Fe}}^{3+}$ EPR*, Phys. Rev. B **34**, 6130 (1986).

[7] A. Bussmann-Holder, H. Beige, and G. Völkel, *Precursor Effects, Broken Local Symmetry, and Coexistence of Order-Disorder and Displacive Dynamics in Perovskite Ferroelectrics*, Phys. Rev. B **79**, 184111 (2009).

[8] W. Zhong, D. Vanderbilt, and K. M. Rabe, *Phase Transitions in $BaTiO_3$ from First Principles*, Phys. Rev. Lett. **73**, 1861 (1994).

[9] R. Comes, M. Lambert, and A. Guinier, *The Chain Structure of BaTiO3 and $KNbO_3$*, Solid State Communications **6**, 715 (1968).

[10] R. Blinc and B. Žekš, *Dynamics of Order-Disorder-Type Ferroelectrics and Anti-Ferroelectrics*, Advances in Physics **21**, 693 (1972).

[11] M. S. Senn, D. A. Keen, T. C. A. Lucas, J. A. Hriljac, and A. L. Goodwin, *Emergence of Long-Range Order in $BaTiO_3$ from Local Symmetry-Breaking Distortions*, Phys. Rev. Lett. **116**, 207602 (2016).

[12] G. H. Kwei, S. J. L. Billinge, S.-W. Cheong, and J. G. Saxton, *Pair-Distribution Functions of Ferroelectric Perovskites: Direct Observation of Structural Ground States*, Ferroelectrics **164**, 57 (1995).

[13] K. Page, T. Proffen, M. Niederberger, and R. Seshadri, *Probing Local Dipoles and Ligand Structure in $BaTiO_3$ Nanoparticles*, Chem. Mater. **22**, 4386 (2010).

[14] B. Ravel, E. A. Stern, R. I. Vedrinskii, and V. Kraizman, *Local Structure and the Phase Transitions of $BaTiO_3$*, Ferroelectrics **206**, 407 (1998).

[15] Y. Qi, S. Liu, I. Grinberg, and A. M. Rappe, *Atomistic Description for Temperature-Driven Phase Transitions in $BaTiO_3$*, Phys. Rev. B **94**, 134308 (2016).

[16] M. Paściak, T. R. Welberry, J. Kulda, S. Leoni, and J. Hlinka, *Dynamic Displacement Disorder of Cubic $BaTiO_3$*, Phys. Rev. Lett. **120**, 167601 (2018).

[17] J.-H. Ko, T. H. Kim, K. Roleder, D. Rytz, and S. Kojima, *Precursor Dynamics in the Ferroelectric Phase Transition of Barium Titanate Single Crystals Studied by Brillouin Light Scattering*, Phys. Rev. B **84**, 094123 (2011).

[18] A. M. Pugachev, V. I. Kovalevskii, N. V. Surovtsev, S. Kojima, S. A. Prosandeev, I. P. Raevski, and S. I. Raevskaya, *Broken Local Symmetry in Paraelectric $BaTiO_3$ Proved by Second Harmonic Generation*, Phys. Rev. Lett. **108**, 247601 (2012).

[19] E. K. H. Salje, X. Ding, and O. Aktas, *Domain Glass*, Physica Status Solidi (b) **251**, 2061 (2014).

[20] S. Hashemizadeh, A. Biancoli, and D. Damjanovic, *Symmetry Breaking in Hexagonal and Cubic Polymorphs of $BaTiO_3$*, Journal of Applied Physics **119**, 094105 (2016).

[21] O. Aktas, S. Crossley, M. A. Carpenter, and E. K. H. Salje, *Polar Correlations and Defect-Induced Ferroelectricity in Cryogenic $KTaO_3$*, Phys. Rev. B **90**, 165309 (2014).

[22] E. K. H. Salje, M. A. Carpenter, G. F. Nataf, G. Picht, K. Webber, J. Weerasinghe, S. Lisenkov, and L. Bellaiche, *Elastic Excitations in $BaTiO_3$ Single Crystals and Ceramics: Mobile Domain Boundaries and Polar Nanoregions Observed by Resonant Ultrasonic Spectroscopy*, Phys. Rev. B **87**, 014106 (2013).

[23] M. Eremenko, V. Krayzman, A. Bosak, H. Y. Playford, K. W. Chapman, J. C. Woicik, B. Ravel, and I. Levin, *Local Atomic Order and Hierarchical Polar Nanoregions in a Classical Relaxor Ferroelectric*, Nature Communications **10**, 1 (2019).

[24] J. Harada, J. D. Axe, and G. Shirane, *Neutron-Scattering Study of Soft Modes in Cubic $BaTiO_3$*, Phys. Rev. B **4**, 155 (1971).

[25] I. Tomeno, J. A. Fernandez-Baca, S. Chi, K. Oka, and Y. Tsunoda, *Coexistence of Soft Modes and Dynamic Ti Disorder in Cubic $BaTiO_3$ Studied by Inelastic Neutron Scattering*, J. Phys. Soc. Jpn. **89**, 054601 (2020).

[26] A. Belsky, M. Hellenbrandt, V. L. Karen, and P. Luksch, *New Developments in the Inorganic Crystal Structure Database (ICSD): Accessibility in Support of Materials Research and Design*, Acta Cryst B Struct Sci Cryst Eng Mater **58**, 364 (2002).

[27] A. Jain, S. P. Ong, G. Hautier, W. Chen, W. D. Richards, S. Dacek, S. Cholia, D. Gunter, D. Skinner, G. Ceder, and K. A. Persson, *Commentary: The Materials Project: A Materials Genome Approach to Accelerating Materials Innovation*, APL Materials **1**, 011002 (2013).

[28] S. Kirklin, J. E. Saal, B. Meredig, A. Thompson, J. W. Doak, M. Aykol, S. Rühl, and C. Wolverton, *The Open Quantum Materials Database (OQMD): Assessing the Accuracy of DFT Formation Energies*, Npj Computational Materials **1**, 15010 (2015).

[29] S. Curtarolo, W. Setyawan, G. L. W. Hart, M. Jahnatek, R. V. Chepulskii, R. H. Taylor, S. Wang, J. Xue, K. Yang, O. Levy, M. J. Mehl, H. T. Stokes, D. O. Demchenko, and D. Morgan, *AFLOW: An Automatic Framework for High-Throughput Materials Discovery*, Computational Materials Science **58**, 218 (2012).

[30] O. I. Malyi and A. Zunger, *False Metals, Real Insulators, and Degenerate Gapped Metals*, Applied Physics Reviews **7**, 041310 (2020).

[31] C. M. I. Okoye, *Theoretical Study of the Electronic Structure, Chemical Bonding and Optical Properties of $KNbO_3$ in the Paraelectric Cubic Phase*, J. Phys.: Condens. Matter **15**, 5945 (2003).

[32] S. Saha, T. P. Sinha, and A. Mookerjee, *Electronic Structure, Chemical Bonding, and Optical Properties of Paraelectric $BaTiO_3$*, Phys. Rev. B **62**, 8828 (2000).

[33] S. Cabuk, H. Akkus, and A. M. Mamedov, *Electronic and Optical Properties of $KTaO_3$: Ab Initio Calculation*, Physica B: Condensed Matter **394**, 81 (2007).

[34] A. Bencan, E. Oveisi, S. Hashemizadeh, V. K. Veerapandiyan, T. Hoshina, T. Rojac, M. Deluca, G. Drazic, and D. Damjanovic, *Atomic Scale Symmetry and Polar Nanoclusters in the Paraelectric Phase of Ferroelectric Materials*, Nat Commun **12**, 1 (2021).

[35] A. Zunger, *Electronic Structure of 3d Transition-Atom Impurities in Semiconductors*, in *Solid State Physics*, edited by H. Ehrenreich and D. Turnbull, Vol. 39 (Academic Press, 1986), pp. 275–464.

[36] A. F. Wells, *Structural Inorganic Chemistry* (OUP Oxford, 2012).

[37] A. Mercy, J. Bieder, J. Íñiguez, and P. Ghosez, *Structurally Triggered Metal-Insulator Transition in Rare-Earth Nickelates*, Nature Communications **8**, 1677 (2017).

[38] R. E. Cohen, *Origin of Ferroelectricity in Perovskite Oxides*, Nature **358**, 136 (1992).

[39] Q. Zhang, T. Cagin, and W. A. Goddard, *The Ferroelectric and Cubic Phases in $BaTiO_3$ Ferroelectrics Are Also Antiferroelectric*, PNAS **103**, 14695 (2006).

[40] M. Kotiuga, S. Halilov, B. Kozinsky, M. Fornari, N. Marzari, and G. Pizzi, *A Microscopic Picture of Paraelectric Perovskites from Structural Prototypes*, arXiv:2107.04628, July 13 (2021).

[41] X.-G. Zhao, G. M. Dalpian, Z. Wang, and A. Zunger, *Polymorphous Nature of Cubic Halide Perovskites*, Phys. Rev. B **101**, 155137 (2020).

[42] X.-G. Zhao, Z. Wang, O. I. Malyi, and A. Zunger, *Effect of Static Local Distortions vs. Dynamic Motions on the Stability and Band Gaps of Cubic Oxide and Halide Perovskites*, Materials Today, **49**, 107-122 (2021).

[43] S. G. Duyker, J. A. Hill, C. J. Howard, and A. L. Goodwin, *Guest-Activated Forbidden Tilts in a Molecular Perovskite Analogue*, J. Am. Chem. Soc. **138**, 11121 (2016).

[44] V. M. Goldschmidt, *Die Gesetze der Krystallochemie*, Naturwissenschaften **14**, 477 (1926).

[45] G. Trimarchi, Z. Wang, and A. Zunger, *Polymorphous Band Structure Model of Gapping in the Antiferromagnetic and Paramagnetic Phases of the Mott Insulators MnO, FeO, CoO, and NiO*, Phys. Rev. B **97**, 035107 (2018).

[46] X. Moya, E. Stern-Taulats, S. Crossley, D. González-Alonso, S. Kar-Narayan, A. Planes, L. Mañosa, and N. D. Mathur, *Giant Electrocaloric Strength in Single-Crystal $BaTiO_3$,* Advanced Materials **25**, 1360 (2013).

[47] G. Burns and F. H. Dacol, *Polarization in the Cubic Phase of BaTIO3*, Solid State Communications **42**, 9 (1982).

[48] A. M. Quittet and M. Lambert, *Temperature Dependence of the Raman Cross Section and Light Absorption in Cubic $BaTiO_3$*, Solid State Communications **12**, 1053 (1973).

[49] J. P. Perdew, K. Burke, and M. Ernzerhof, *Generalized Gradient Approximation Made Simple*, Phys. Rev. Lett. **77**, 3865 (1996).

[50] G. Kresse and J. Furthmüller, *Efficiency of Ab-Initio Total Energy Calculations for Metals and Semiconductors Using a Plane-Wave Basis Set*, Computational Materials Science **6**, 15 (1996).

[51] G. Kresse and J. Furthmüller, *Efficient Iterative Schemes for Ab initio Total-Energy Calculations Using a Plane-Wave Basis Set*, Phys. Rev. B **54**, 11169 (1996).

[52] X.-G. Zhao, K. Zhou, B. Xing, R. Zhao, S. Luo, T. Li, Y. Sun, G. Na, J. Xie, X. Yang, X. Wang, X. Wang, X. He, J. Lv, Y. Fu, and L. Zhang, *JAMIP: An Artificial-Intelligence Aided Data-Driven Infrastructure for Computational Materials Informatics*, Science Bulletin **66**, 1973 (2021).

[53] J. Sun, A. Ruzsinszky, and J. P. Perdew, *Strongly Constrained and Appropriately Normed Semilocal Density Functional*, Phys. Rev. Lett. **115**, 036402 (2015).

[54] W. G. Hoover, A. J. C. Ladd, and B. Moran, *High-Strain-Rate Plastic Flow Studied via Nonequilibrium Molecular Dynamics*, Phys. Rev. Lett. **48**, 1818 (1982).

[55] O. L. G. Alderman, C. J. Benmore, J. Neuefeind, A. Tamalonis, and R. Weber, *Molten Barium Titanate: A High-Pressure Liquid Silicate Analogue*, J. Phys.: Condens. Matter **31**, 20LT01 (2019).

[56] C. Moriyoshi, S. Hiramoto, H. Ohkubo, Y. Kuroiwa, H. Osawa, K. Sugimoto, S. Kimura, M. Takata, Y. Kitanaka, Y. Noguchi, and M. Miyayama, *Synchrotron Radiation Study on Time-Resolved Tetragonal Lattice Strain of $BaTiO_3$ under Electric Field*, Jpn. J. Appl. Phys. **50**, 09NE05 (2011).

[57] P. V. Balachandran, N. A. Benedek, and J. M. Rondinelli, *Symmetry-Adapted Distortion Modes as Descriptors for Materials Informatics*, in *Information Science for Materials Discovery and Design*, edited by T. Lookman, F. J. Alexander, and K. Rajan (Springer International Publishing, Cham, 2016), pp. 213–222.

[58] B. J. Campbell, H. T. Stokes, D. E. Tanner, and D. M. Hatch, *ISODISPLACE: A Web-Based Tool for Exploring Structural Distortions*, J Appl Cryst **39**, 607 (2006).